JOURNAL OF COMPUTATIONAL PHYSICS **124,** 417–430 (1996)
ARTICLE NO. 0069

# An Adiabatic Fluid Electron Particle-in-Cell Code for Simulating Ion-Driven Parametric Instabilities*

H. X. VU

*Applied Theoretical and Computational Division, Los Alamos National Laboratory, Los Alamos, New Mexico 87545*

Received February 9, 1995

A hybrid particle-in-cell (PIC) method is presented in which the electrons are modeled as an adiabatic fluid with an arbitrary ratio of specific heats $\gamma$. The electromagnetic field model is based on a temporal Wentzel–Krammers–Brillouin approximation. The method is a new tool for simulating ion-driven parametric instabilities which often exist in laser-produced plasmas. The method is general and does not depend on the number of spatial dimensions. The method will model the plasma behavior correctly even in situations where the electron Debye shielding is not negligible. Test simulations of ion Landau damping in both one and two dimensions are performed, and the results are in excellent agreement with linear Vlasov theory. Test simulations of stimulated Brillouin scattering (SBS) in one and two dimensions are performed, and the results indicate that when the intensity of the driving electromagnetic field is sufficiently high, backscatter SBS is dominant at early time while side-scatter SBS is dominant at late time. For the test cases in which a high-frequency driving electromagnetic field is present, our hybrid PIC method offers a substantial saving in computational time over explicit PIC methods that require the time scale of the driving electromagnetic field to be resolved. 

## 1. INTRODUCTION

Particle simulation of plasmas has been a challenging effort for the past several decades [1]. Self-consistent plasma behavior is often nonlinear and involves many highly disparate temporal and spatial scales simultaneously. The differing temporal and spatial scales arise from the fact that the electrons and ions have very different masses ($m_i/m_e \geq 1836$), and therefore have highly different responses to electromagnetic forces. A variety of time-explicit, time-implicit, and hybrid particle-in-cell (PIC) algorithms exist in the literature for solving the coupled Maxwell–Vlasov equations [2–18]. Each PIC algorithm has its share of merits as well as deficiencies, and there is not a universal approach that is suitable for all problems. One must therefore decide on an approach that is most suitable for one's particular needs. For example, one may need to model a plasma instability which grows and saturates on the electron time scale. If the electron time scale is the fastest time scale of the system, it is then appropriate to use the time-explicit PIC algorithms [19] because they are efficient and easy to use. The only constraint imposed by time-explicit algorithms is that one must resolve the fastest time scale in order to achieve numerical stability. However, this constraint places no additional burden on one's computing resources since one must, in this particular situation, resolve the fastest time scale in order to model the physics correctly. If, on the other hand, one wishes to model a physical process which varies on the ion time scale, either the time-implicit algorithms [20] or the hybrid algorithms [21] may be appropriate, depending on whether electron kinetic effects are deemed important.

In the presence of an external driving electromagnetic wave, an additional time scale is introduced, i.e., the frequency of the external field. The time scale of the external field is often very fast compared to the electron time scale. For instance, in inertial confinement fusion (ICF) research, the frequency of the pump laser is typically several times faster than the electron plasma frequency which, in turn, is an order of magnitude faster than the ion time scale. It is in the area of ICF research that this report focuses its attention. In laser-driven plasmas, several types of parametric instabilities exist [22], driven by electron and ion kinetic effects. To model electron-driven parametric instabilities, e.g., stimulated Raman scattering (SRS), which grows and saturates on the electron time scale, time-explicit PIC algorithms can be used [23]. In this case, one must resolve the laser frequency in order to obtain numerically stable solutions. However, since the laser frequency is only several times faster than the growth rate of the instabilities, the computational cost of such a simulation is tolerable. A new, and more efficient, method for simulating SRS was recently proposed [24] in which the electromagnetic wave is modeled by a Wentzel–Krammers–Brillouin (WKB) field envelope in both space and time. Because the temporal and spatial scales associated with the driving electromagnetic field have been removed by virtue of the spatial and temporal WKB representation, SRS can be modeled on the electron time scale. The disadvantage with this new

* The U.S. Government's right to retain a nonexclusive royalty-free license in and to the copyright covering this paper, for governmental purposes, is acknowledged.



0021-9991/96 $18.00

method is that it does not allow for side-scattering in two or three dimensions.

To model ion-driven parametric instabilities, e.g., stimulated Brillouin scattering (SBS), which occur on the ion time scale, it is not computationally efficient to resolve the laser frequency. Attempts to model SBS with a time-explicit PIC model in which the electromagnetic wave and the electrons are subcycled have yielded some success [25]. However, such simulations have been confined to one spatial dimension. A more efficient approach is to use a quasi-neutral hybrid PIC algorithm in which the ion kinetic effects are retained by treating the ions as finite-size particles, and the electrons are treated as a fluid whose motion is such that the plasma remains quasi-neutral at all times [26]. For physical situations in which the electron Debye shielding is unimportant, this approach is suitable. However, for situations in which the electron Debye shielding is significant, as is the case for the current ICF regime of interest ($k\lambda_{De} = O(1)$), this approach is deficient because it does not model the electron Debye shielding correctly.

In this paper, we propose a hybrid PIC algorithm in which the ions are treated as finite-size particles. The electrons are modeled as an adiabatic fluid with an arbitrary ratio of specific heats $\gamma$. The electromagnetic wave is modeled using a temporal WKB analysis and results in a Schrodinger-like equation for the slowly varying wave envelope. The plasma is required to be globally charge neutral, although it is not required to be locally quasi-neutral. This method offers the advantage that the electron Debye shielding is modeled correctly. Furthermore, since one has not invoked a WKB approximation in space, the method can model SBS in any direction. The method is also capable of modeling the interaction between SBS and the filamentation instability (FI). In the absence of the pump electromagnetic wave, our hybrid PIC model, with $\gamma = 1$, reduces to a widely used model discussed elsewhere [19].

The rest of this paper is divided into four sections. In Section 2 we described the physical model appropriate for simulating ion-driven parametric instabilities. The numerical algorithm for advancing the governing equations in time and its numerical properties are discussed in Section 3. In Section 4, test simulations of ion Landau damping and SBS in one and two dimensions are presented, and the simulation results are compared against linear Vlasov theory. Section 5 is a summary of our results and the conclusions based on these results.

## 2. PHYSICAL MODEL

In the presence of an electromagnetic pump wave of frequency $\omega_0$, the vector potential $\mathbf{A}(\mathbf{x}, t)$ within the plasma can be written as

$$\mathbf{A}(\mathbf{x}, t) = \tfrac{1}{2}(\mathbf{a}(\mathbf{x}, t)e^{-i\omega_0 t} + \mathbf{a}^*(\mathbf{x}, t)e^{i\omega_0 t}), \tag{1}$$

where $\mathbf{a}(\mathbf{x}, t)$ is complex-valued. The vector $\mathbf{a}$ is assumed to vary on a time scale much longer than $2\pi/\omega_0$. The electron's equation of motion:

$$m_e \frac{d\mathbf{u}}{dt} = -e\left(\mathbf{E} + \frac{\mathbf{u} \times \mathbf{B}}{c}\right) \tag{2}$$

can be solved iteratively as follows. First, by neglecting the $\mathbf{u} \times \mathbf{B}$ force, one can solve approximately for the transverse component of $\mathbf{u}$:

$$\mathbf{u}_T \simeq \frac{e\mathbf{A}}{m_e c}. \tag{3}$$

Substituting Eq. (3) into the right-hand side of Eq. (2), one obtains

$$\begin{aligned} m_e \frac{d\mathbf{u}}{dt} \simeq & -e\left(-\nabla\phi + \frac{\mathbf{u}_L \times \mathbf{B}}{c}\right) \\ & - \frac{e^2}{m_e c^2}\left[\frac{1}{2}\nabla(\mathbf{A} \cdot \mathbf{A}) - \nabla \cdot (\mathbf{AA})\right], \end{aligned} \tag{4}$$

where $\mathbf{u}_L$ is the longitudinal component of $\mathbf{u}$. In this paper, we shall consider only the case for which $\nabla \cdot (\mathbf{AA}) = 0$. For instance, in one dimension, this can be achieved by restricting the electric field to the plane normal to the axis of the simulation. In two dimensions, this can be achieved by requiring that the electric field is linearly polarized, and is in the direction normal to the plane of the simulation. In order to remove the fast time scale $2\pi/\omega_0$ from the model, Eq. (4) is averaged over a time interval of $2\pi/\omega_0$, and the resulting equation is

$$m_e \frac{d\mathbf{u}_L}{dt} \simeq e\nabla\phi - \frac{e^2}{4m_e c^2}\nabla(\mathbf{a} \cdot \mathbf{a}^*), \tag{5}$$

where one has made use of the fact that the longitudinal velocity $\mathbf{u}_L$ and the electrostatic potential $\phi$ vary on a time scale much longer than $2\pi/\omega_0$. Although the transverse velocity $\mathbf{u}_T$ varies rapidly in time, it results in a zero average value. The fluid electron momentum equation, valid on a time scale much longer than $2\pi/\omega_0$, can be cast in the form

$$en_e\nabla\phi - \frac{e^2 n_e}{4m_e c^2}\nabla(\mathbf{a} \cdot \mathbf{a}^*) - \nabla p_e = 0, \tag{6}$$

where one has the neglected contribution of the inertial terms in the momentum equation. In our model, we propose to describe the electrons as an adiabatic fluid, i.e., $p_e = n_{e0}T_{e0}(n_e/n_{e0})^\gamma$. $n_{e0}$ and $T_{e0}$ are the initial electron density and temperature, and $\gamma$ is the ratio of specific heats.

The fluid electron momentum equation, Eq. (6), can then be integrated, and the result is

$$e\phi - \frac{e^2}{4m_e c^2}\mathbf{a}\cdot\mathbf{a}^* - f(\gamma, n_e) = \alpha \tag{7}$$

$$f(\gamma, n_e) = \begin{cases} T_{e0}\ln\left(\dfrac{n_e}{n_{e0}}\right) & \text{if } \gamma = 1 \\ T_{e0}\left(\dfrac{\gamma}{\gamma-1}\right)\left(\dfrac{n_e}{n_{e0}}\right)^{\gamma-1} & \text{if } \gamma \neq 1, \end{cases}$$

where $\alpha$ is the constant of integration. Equations (7), with $\gamma = 1$, have been used previously to study rarefaction shocks in a laser-plasma corona by Bezzerides *et al.* [27]. The electrostatic potential $\phi$ is given by Poisson's equation,

$$\nabla^2\phi = 4\pi e\left(n_e - \sum_i Z_i n_i\right), \tag{8}$$

where $Z_i$ and $n_i$ are the ionization state and the density of the $i$th ion species. It is clear from Eqs. (7) and (8) that in order for the plasma to be globally charge neutral, the constant of integration $\alpha$ must be chosen:

$$\int \boldsymbol{\nabla}\phi \cdot d\boldsymbol{\sigma} = 0, \tag{9}$$

where $d\boldsymbol{\sigma}$ is a surface area element. It should be noted that for each ion species $i$, an approximate expression for the ion transverse velocity can also be derived:

$$\mathbf{u}_{i\mathrm{T}} \simeq -\frac{Z_i e\mathbf{A}}{m_i c}. \tag{10}$$

Ampere's law, $\boldsymbol{\nabla}\times\mathbf{B} = (4\pi/c)\mathbf{J}_\mathrm{T} + (1/c)\partial\mathbf{E}_\mathrm{T}/\partial t$, is combined with Eqs. (2) and (10) to give

$$-\nabla^2\mathbf{A} = -\frac{1}{c^2}\frac{\partial^2\mathbf{A}}{\partial t^2} - \frac{1}{c^2}\left(\frac{4\pi e^2 n_e}{m_e} + \sum_i \frac{4\pi e^2 Z_i^2 n_i}{m_i}\right)\mathbf{A}.$$

Substituting Eq. (1) into the above equation, one obtains an equation for $\mathbf{a}(\mathbf{x}, t)$:

$$-\frac{1}{c^2}\frac{\partial^2\mathbf{a}}{\partial t^2} + i\left(\frac{2\omega_0}{c^2}\right)\frac{\partial\mathbf{a}}{\partial t} + \nabla^2\mathbf{a} + \frac{1}{c^2}\left[\omega_0^2 - \left(\frac{4\pi e^2 n_e}{m_e} + \sum_i \frac{4\pi e^2 Z_i^2 n_i}{m_i}\right)\right]\mathbf{a} = 0.$$

Invoking the assumption that $\mathbf{a}$ varies on a time scale much slower than $2\pi/\omega_0$, the above equation can be approximated as

$$i\left(\frac{2\omega_0}{c^2}\right)\frac{\partial\mathbf{a}}{\partial t} + \nabla^2\mathbf{a} + K^2\mathbf{a} = 0$$

$$K^2 \equiv \frac{1}{c^2}\left[\omega_0^2 - (\omega_p^2 + \Omega_p^2)\right] \tag{11}$$

$$\omega_p^2 \equiv \frac{4\pi e^2 n_e}{m_e}$$

$$\Omega_p^2 \equiv \sum_i \frac{4\pi e^2 Z_i^2 n_i}{m_i}.$$

In our model, the ions are treated as individual particles, permitting ion kinetic effects, e.g., Landau damping, to be included in the simulation self-consistently. The ion particle equations of motion,

$$m_i\frac{d\mathbf{u}_{i\mathrm{L}}}{dt} = -eZ_i\boldsymbol{\nabla}\phi - \frac{e^2 Z_i^2}{4m_i c^2}\boldsymbol{\nabla}(\mathbf{a}\cdot\mathbf{a}^*)$$

$$\frac{d\mathbf{x}_i}{dt} = \mathbf{u}_{i\mathrm{L}}, \tag{12}$$

together with Eqs. (7)–(9) and (11), constitute our physical model.

## 3. NUMERICAL ALGORITHM

Because the physical model described by Eqs. (7)–(9) and (11)–(12) is highly nonlinear, one must be extra careful in advancing the equations in order to ensure numerical stability. A temporal discretization scheme and its accompanying nonlinear numerical analysis are presented in which the numerical solutions are shown to be stable, provided that $\Omega_p\delta t < 1$. The spatial discretization of the equations will also be discussed. Before going further, an overview of the algorithm is in order. Each ion particle carries a charge $q_p$, position $\mathbf{x}_p$, and velocity $\mathbf{u}_{p\mathrm{L}}$. Associated with each particle is an interpolation function $S(\mathbf{x} - \mathbf{x}_p)$ that determines how the particle charges are interpolated onto the computational mesh. In our method, $S(\mathbf{x})$ is chosen to be the quadratic B-spline [2]. The electron fluid density $n_e(\mathbf{x}, t)$, electrostatic potential $\phi(\mathbf{x}, t)$, and vector potential $\mathbf{a}(\mathbf{x}, t)$ are determined by solving Eqs. (7)–(9) and (11). The ion density $n_i(\mathbf{x}, t)$, on the other hand, is determined by interpolating the ion charges onto the computational mesh [2], i.e.,

$$eZ_i n_i(\mathbf{x}, t) = \sum_{p\in i} q_p S(\mathbf{x}(t) - \mathbf{x}_p).$$

The ion positions and velocities evolve in time according to Eqs. (12).

A. *Temporal Discretization*

Using the leapfrog algorithm in which the pair of variables $\mathbf{x}$ and $\mathbf{u}_{p\mathrm{L}}$ are advanced in time alternately [19], the ion equations of motion, Eq. (12), are approximated as

$$\frac{\mathbf{u}_{p\mathrm{L}}^{(n+1/2)} - \mathbf{u}_{p\mathrm{L}}^{(n-1/2)}}{\delta t} = -\frac{eZ_i}{m_i}\nabla\phi^{(n)} - \left(\frac{eZ_i}{2m_i c}\right)^2 \nabla(\mathbf{a}^{(n)} \cdot \mathbf{a}^{*(n)})$$

$$\frac{\mathbf{x}_p^{(n+1)} - \mathbf{x}_p^{(n)}}{\delta t} = \mathbf{u}_{p\mathrm{L}}^{(n+1/2)}, \tag{13}$$

where the superscripts $(n - 1/2)$, $(n)$, $(n + 1/2)$, and $(n + 1)$ refer to the time levels $t_n - \delta t/2$, $t_n$, $t_n + \delta t/2$, and $t_{n+1}$, where $t_n \equiv n\delta t$. The electrostatic field equations, Eqs. (7)–(9), are simply evaluated at the time level $n$:

$$e\phi^{(n)} - \frac{e^2}{4m_e c^2}\mathbf{a}^{(n)} \cdot \mathbf{a}^{*(n)} - f(\gamma, n_e^{(n)}) = \alpha^{(n)} \tag{14}$$

$$\nabla^2\phi^{(n)} = 4\pi e\left(n_e^{(n)} - \sum_i Z_i n_i^{(n)}\right)$$

$$\int \nabla\phi^{(n)} \cdot d\boldsymbol{\sigma} = 0. \tag{15}$$

Using the Crank–Nicolson method, the electromagnetic field equation, Eq. (11), is advanced in time as

$$i\left(\frac{2\omega_0}{c^2}\right)\frac{\mathbf{a}^{(n)} - \mathbf{a}^{(n-1)}}{\delta t} + \frac{1}{2}\nabla^2(\mathbf{a}^{(n)} + \mathbf{a}^{(n-1)}) + \frac{1}{4}([K^{(n)}]^2 + [K^{(n-1)}]^2)(\mathbf{a}^{(n)} + \mathbf{a}^{(n-1)}) = 0, \tag{16}$$

where

$$[K^{(n)}]^2 = \omega_0^2 - [\omega_p^{(n)}]^2 - [\Omega_p^{(n)}]^2,$$

$$[K^{(n-1)}]^2 = \omega_0^2 - [\omega_p^{(n-1)}]^2 - [\Omega_p^{(n-1)}]^2$$

$$[\omega_p^{(n)}]^2 = \frac{4\pi e^2 n_e^{(n)}}{m_e},$$

$$[\omega_p^{(n-1)}]^2 = \frac{4\pi e^2 n_e^{(n-1)}}{m_e}$$

$$[\Omega_p^{(n)}]^2 = \sum_i \frac{4\pi e^2 Z_i^2 n_i^{(n)}}{m_i},$$

$$[\Omega_p^{(n-1)}]^2 = \sum_i \frac{4\pi e^2 Z_i^2 n_i^{(n-1)}}{m_i}$$

$$eZ_i n_i^{(n)} = \sum_{p\in i} q_p S(\mathbf{x} - \mathbf{x}_p^{(n)}),$$

$$eZ_i n_i^{(n-1)} = \sum_{p\in i} q_p S(\mathbf{x} - \mathbf{x}_p^{(n-1)}).$$

Recall that $\alpha^{(n)}$ is the constant of integration at time $t$. Equation (15) is the constraint that $\alpha^{(n)}$ must satisfy in order to maintain global charge neutrality.

In the absence of the pump electromagnetic field represented by $\mathbf{a}(\mathbf{x}, t)$, our model, with $\gamma = 1$, reduces to the standard Boltzmann fluid electron model. The leapfrog algorithm, Eqs. (13)–(14), is well known and has been shown in past literature to be numerically stable. We will therefore concentrate our effort on the nonlinear stability analysis of Eq. (16). Note that for the special case in which $K$ is independent of $\mathbf{a}$, the analysis is straightforward, and Eq. (16) can be shown to be unconditionally stable and second-order accurate in time. However, for the general case in which $K^{(n)}$ is an implicit and nonlinear function of $\mathbf{a}^{(n)}$, as can be seen from Eqs. (13)–(15), the analysis is somewhat more complicated. Multiplying Eq. (16) by $(\mathbf{a}^{*(n)} + \mathbf{a}^{*(n-1)})/2$ and subtracting the resulting equation from its complex conjugate, one obtains the equation

$$i\left(\frac{2\omega_0}{c^2}\right)\frac{\mathbf{a}^{(n)} \cdot \mathbf{a}^{*(n)} - \mathbf{a}^{(n-1)} \cdot \mathbf{a}^{*(n-1)}}{\delta t} + \frac{1}{2}(\mathbf{a}^{*(n)} + \mathbf{a}^{*(n-1)}) \cdot \nabla^2(\mathbf{a}^{(n)} + \mathbf{a}^{(n-1)}) - \frac{1}{2}(\mathbf{a}^{(n)} + \mathbf{a}^{(n-1)}) \cdot \nabla^2(\mathbf{a}^{*(n)} + \mathbf{a}^{*(n-1)}) = 0. \tag{17}$$

Assuming a solution of the form $\mathbf{a}^{(n)} = A\mathbf{a}^{(n-1)}$, where $A$ is the amplification factor, and Fourier analyzing the above equation, one obtains

$$AA^* = 1.$$

Since above equation for the amplification factor $A$ holds true independently of the time step $\delta t$, Eq. (16) is unconditionally stable.

Equation (17) can be recast in a more convenient form as

$$\frac{\mathbf{a}^{(n)} \cdot \mathbf{a}^{*(n)} - \mathbf{a}^{(n-1)} \cdot \mathbf{a}^{*(n-1)}}{\delta t} + \nabla \cdot \mathbf{F}^{(n+1/2)} = 0, \tag{18}$$

where

$$\mathbf{F}^{(n+1/2)} \equiv -i\left(\frac{c^2}{\omega_0}\right)(\mathbf{a}^{*(n+1/2)} \cdot \nabla\mathbf{a}^{(n+1/2)} - \mathbf{a}^{(n+1/2)} \cdot \nabla\mathbf{a}^{*(n+1/2)})$$

$$\mathbf{a}^{(n+1/2)} \equiv \frac{1}{2}(\mathbf{a}^{(n)} + \mathbf{a}^{(n-1)}).$$

Equation (18) is just a time-discrete energy conservation law for the electromagnetic wave energy density. Here,

$\mathbf{a}^{(n)} \cdot \mathbf{a}^{*(n)}$ is the energy density of the electromagnetic wave at time level $t_n$, and $\mathbf{F}^{(n+1/2)}$ is the energy flux at time level $t_{n+1/2}$. By integrating this energy equation over the volume of the simulation, one can readily show that in the absence of a net energy flux through the boundary, the wave energy is conserved exactly from time step to time step. In the presence of a net energy flux through the boundary, the energy gained or lost by the wave is equal to the net energy crossing the boundary in any given time step. From the above time-discrete energy conservation law, one can show that the Crank–Nicholson algorithm for the nonlinear problem, Eq. (16), is second-order accurate in time.

B. *Spatial Discretization*

The physical model described by Eqs. (7)–(9) and (11)–(12) and its time-discrete representation, Eqs. (13)–(16), are valid in any spatial geometry (one, two, and three spatial dimensions), provided that the condition $\nabla \cdot (\mathbf{AA}) = 0$ is satisfied. For the purpose of illustration, only the simplest two-dimensional spatial discretization is described.

Equations (13)–(16) are solved in a rectangular region with $0 \le x \le L_x$ and $0 \le y \le L_y$. The computational mesh is staggered and consists of $N_x \times N_y$ rectangular cells of equal size. $\mathbf{x}^v_{kl}$, the physical coordinate of the vertices of the computation cells, and $\mathbf{x}^c_{kl}$, the physical coordinate of the centers of the computational cells, are specified as

$$\mathbf{x}^v_{kl} = (k-1)\delta x \hat{\mathbf{e}}_x + (l-1)\delta y \hat{\mathbf{e}}_y$$

$$\mathbf{x}^c_{kl} = \mathbf{x}^v_{kl} + \frac{\delta x}{2}\hat{\mathbf{e}}_x + \frac{\delta y}{2}\hat{\mathbf{e}}_y,$$

where $\delta x \equiv L_x/(N_x - 1)$ and $\delta y \equiv L_y/(N_y - 1)$; $k$ and $l$ are indices labelling the computational cells.

The electron density $n_e$, ion density $n_i$, electrostatic potential $\phi$, and the pump electromagnetic field $\mathbf{a}$ are cell-centered quantities. The ion density $n_i^{(n)}$ is computed from known particle data as

$$n^{(n)}_{i,kl} = \sum_{p \in i} q_p S(\mathbf{x}^c_{kl} - \mathbf{x}^{(n)}_p). \tag{19}$$

The spatially discrete representations of Eqs. (14)–(16) are

$$e\phi^{(n)}_{kl} - \frac{e^2}{4m_e c^2}\mathbf{a}^{(n)}_{kl} \cdot \mathbf{a}^{*(n)}_{kl} - f(\gamma, n^{(n)}_{e,kl}) = \alpha^{(n)}$$

$$D_{kl}[\phi^{(n)}] = 4\pi e\left(n^{(n)}_{e,kl} - \sum_i Z_i n^{(n)}_{i,kl}\right) \tag{20}$$

$$\delta x \sum_{k=1}^{N_x - 1}\left(\frac{\phi^{(n)}_{kN_y} - \phi^{(n)}_{kN_y-1}}{\delta y} - \frac{\phi^{(n)}_{k1} - \phi^{(n)}_{k0}}{\delta y}\right) + \delta y \sum_{l=1}^{N_y - 1}\left(\frac{\phi^{(n)}_{N_x l} - \phi^{(n)}_{N_x - 1 l}}{\delta x} - \frac{\phi^{(n)}_{1l} - \phi^{(n)}_{0l}}{\delta x}\right) = 0 \tag{21}$$

$$i\left(\frac{2\omega_0}{c^2}\right)\frac{\mathbf{a}^{(n)}_{kl} - \mathbf{a}^{(n-1)}_{kl}}{\delta t} + \frac{1}{2}\left(D_{kl}[\mathbf{a}^{(n)}] + D_{kl}[\mathbf{a}^{(n-1)}]\right) + \frac{1}{4}\left([K^{(n)}_{kl}]^2 + [K^{(n-1)}_{kl}]^2\right)\left(\mathbf{a}^{(n)}_{kl} + \mathbf{a}^{(n-1)}_{kl}\right) = 0, \tag{22}$$

where the numerical Laplacian operator is defined as

$$D_{kl}[\phi^{(n)}] \equiv \frac{\phi^{(n)}_{k+1l} - 2\phi^{(n)}_{kl} + \phi^{(n)}_{k-1l}}{(\delta x)^2} + \frac{\phi^{(n)}_{kl+1} - 2\phi^{(n)}_{kl} + \phi^{(n)}_{kl-1}}{(\delta y)^2}.$$

It should be noted here that $\phi^{(n)}_{kN_y}$, $\phi^{(n)}_{k0}$, $\phi^{(n)}_{N_x l}$, and $\phi^{(n)}_{0l}$ refer to values of $\phi^{(n)}$ in the ghost cells.

Equations (20)–(22) form a formidable set of nonlinear coupled equations which one must solve in order to obtain $n_e^{(n)}$, $\phi^{(n)}$, $\mathbf{a}^{(n)}$, and $\alpha^{(n)}$. An efficient method for solving these coupled equations will be presented in the next section. Upon obtaining solutions for $\phi^{(n)}$ and $\mathbf{a}^{(n)}$, the ion particles are advanced in time using a spatially discrete representation of Eqs. (13),

$$\frac{\mathbf{u}^{(n+1/2)}_{p\mathrm{L}} - \mathbf{u}^{(n-1/2)}_{p\mathrm{L}}}{\delta t} = -\frac{eZ_i}{m_i}\tilde{\mathbf{E}}^{(n)}_p$$

$$\frac{\mathbf{x}^{(n+1)}_p - \mathbf{x}^{(n)}_p}{\delta t} = \mathbf{u}^{(n+1/2)}_{p\mathrm{L}}, \tag{23}$$

where

$$\tilde{\mathbf{E}}^{(n)}_p = (1-\eta)(1-\xi)\mathbf{E}^{(n)}_{kl} + \eta(1-\xi)\mathbf{E}^{(n)}_{k+1l} + (1-\eta)\xi\mathbf{E}^{(n)}_{k,l+1} + \eta\xi\mathbf{E}^{(n)}_{k+1l+1}$$

$$\mathbf{E}^{(n)}_{kl} \equiv \frac{1}{2}\left(\frac{\Phi^{(n)}_{kl} - \Phi^{(n)}_{k-1l}}{\delta x} + \frac{\Phi^{(n)}_{kl-1} - \Phi^{(n)}_{k-1l-1}}{\delta x}\right)\hat{\mathbf{e}}_x + \frac{1}{2}\left(\frac{\Phi^{(n)}_{kl} - \Phi^{(n)}_{kl-1}}{\delta y} + \frac{\Phi^{(n)}_{k-1l} - \Phi^{(n)}_{k-1l-1}}{\delta y}\right)\hat{\mathbf{e}}_y$$

$$\Phi^{(n)} \equiv \phi^{(n)} + \frac{eZ_i}{4m_i c^2}\mathbf{a}^{(n)} \cdot \mathbf{a}^{*(n)}$$

$$\eta \equiv \left(\frac{\mathbf{x}^{(n)}_p - \mathbf{x}^v_{kl}}{\delta x}\right) \cdot \hat{\mathbf{e}}_x$$

$$\xi \equiv \left(\frac{\mathbf{x}^{(n)}_p - \mathbf{x}^v_{kl}}{\delta y}\right) \cdot \hat{\mathbf{e}}_y.$$

The indices $k$ and $l$ must be chosen such that $0 \le \eta < 1$ and $0 \le \xi < 1$.

C. *Method for Solving Field Equations*

An iterative algorithm for solving Eqs. (20)–(22) is presented. An obvious approach would be to solve these equations as a set of nonlinear coupled equations by means of the Newton–Raphson algorithm in which the equations are linearized about an approximate solution and the correction to the approximate solution is obtained by solving the resulting set of linear equations [28]. Such an approach would be appropriate if the coupling of the computational mesh points were local, e.g., a five-point or nine-point stencil in two dimensions. A more careful examination of Eq. (21) reveals the global nature of this equation, i.e., Eq. (21) couples all of the computational mesh points that are immediately adjacent to the physical boundaries. Because of this nonlocal coupling of the mesh points, a straightforward application of the Newton–Raphson algorithm is not appropriate. Here, a modified version of the Newton–Raphson algorithm is proposed in which Eqs. (20)–(22) are solved using three nested Newton–Raphson iterative steps. In effect, we have devised a splitting algorithm in which Eqs. (20), (21), and (22) are decoupled from each other. The price one has to pay is the two iteration levels in addition to the standard Newton–Raphson iteration. However, because the algorithm requires only a few iterations to converge, the additional cost is not significant. With this modified Newton–Raphson algorithm, the nonlocal coupling of mesh points due to Eq. (21) is a rather trivial issue.

Let the non-negative integer indices $m_1$, $m_2$, and $m_3$ denote the iteration cycle of the outermost, intermediate, and innermost Newton–Raphson iteration level, respectively. Furthermore, let $\Theta$ be an arbitrary quantity whose value at time $t$ is denoted by $\Theta^{(n)}$. Then, $\tilde{\Theta}^{(m_1)}$, $\hat{\Theta}^{(m_1,m_2)}$, and $\overline{\Theta}^{(m_1,m_2,m_3)}$ refer to approximations of $\Theta^n$ in the outermost, intermediate, and innermost iteration level, respectively. Assuming that all three levels of Newton–Raphson iterations are convergent, the relationship between these various representations of $\Theta^{(n)}$ can be expressed as

$$\lim_{m_3\to\infty} \overline{\Theta}^{(m_1,m_2,m_3)} = \hat{\Theta}^{(m_1,m_2)}$$
$$\lim_{m_2\to\infty} \hat{\Theta}^{(m_1,m_2)} = \tilde{\Theta}^{(m_1)}$$
$$\lim_{m_1\to\infty} \tilde{\Theta}^{(m_1)} = \Theta^{(n)}.$$

Because the overall algorithm for solving Eqs. (20)–(22) is somewhat complicated, its presentation is done in two parts. First, Eqs. (20)–(22) are linearized in the order that these equations are used. Second, for the purpose of clarity, a typical computational cycle in which all of the variables are advanced in time is described in detail with references to the linearized equations.

Linearizing Eq. (22), one obtains

$$\left.\begin{aligned} & i\left(\frac{2\omega_0}{c^2\delta t}\right)\delta\tilde{\mathbf{a}}^{(m_1)} + \frac{1}{2}D[\delta\tilde{\mathbf{a}}^{(m_1)}] \\ & + \frac{1}{2}\left[\frac{\partial[\tilde{K}^{(m_1)}]^2}{\partial\tilde{\mathbf{a}}^{(m_1)}}\cdot\delta\tilde{\mathbf{a}}^{(m_1)}\right]\tilde{\mathbf{a}}^{(m_1)} \\ & + \frac{1}{4}([\tilde{K}^{(m_1)}]^2 + [K^{(n-1)}]^2)\delta\tilde{\mathbf{a}}^{(m_1)} \end{aligned}\right\}$$
$$= \begin{cases} -i\left(\dfrac{2\omega_0}{c^2\delta t}\right)(\tilde{\mathbf{a}}^{(m_1)} - \mathbf{a}^{(n-1)}) \\ -\dfrac{1}{2}(D[\tilde{\mathbf{a}}^{(m_1)}] + D[\mathbf{a}^{(n-1)}]) \\ -\dfrac{1}{4}([\tilde{K}^{(m_1)}]^2 + [K^{(n-1)}]^2)(\tilde{\mathbf{a}}^{(m_1)} + \mathbf{a}^{(n-1)}) \end{cases} \tag{24a}$$

$$\tilde{\mathbf{a}}^{(m_1+1)} = \begin{cases} \mathbf{a}^{(n-1)} & \text{if } m_1 + 1 = 0 \\ \tilde{\mathbf{a}}^{(m_1)} + \delta\tilde{\mathbf{a}}^{(m_1)} & \text{if } m_1 + 1 > 0, \end{cases} \tag{24b}$$

where the indices $k$ and $l$ are understood to be in the above equation; i.e., the above equation is to be applied at every point on the computational mesh. In order to obtain $\mathbf{a}^{(n)}$, the above iterative algorithm is carried out until convergence is achieved, i.e.,

$$\lim_{\varepsilon_{\tilde{\mathbf{a}}}^{(m_1)}\to 0} \tilde{\mathbf{a}}^{(m_1)} = \mathbf{a}^{(n)}$$
$$\varepsilon_{\tilde{\mathbf{a}}}^{(m_1)} \equiv \left\|\sqrt{\delta\tilde{\mathbf{a}}^{(m_1)}\cdot\delta\tilde{\mathbf{a}}^{*(m_1)}}\right\|_\infty \Big/ \left\|\sqrt{\tilde{\mathbf{a}}^{(m_1)}\cdot\tilde{\mathbf{a}}^{(m_1)}}\right\|_\infty. \tag{25}$$

Equations (24)–(25) allow one to compute $\mathbf{a}^{(n)}$, provided that $[\tilde{K}^{(m_1)}]^2$ is known for all values of $m_1$ required by these equations in order for numerical convergence to be achieved. Note that in Eq. (24a), although $\partial[\tilde{K}^{(m_1)}]^2/\partial\tilde{\mathbf{a}}^{(m_1)}$ is not known explicitly, it can be readily approximated by numerically computing $\tilde{K}^2$ at two slightly displaced values of $\tilde{\mathbf{a}}$ (centered about $\tilde{\mathbf{a}}^{(m_1)}$) and forming the gradient of $\tilde{K}^2$ with respect to $\tilde{\mathbf{a}}$ numerically.

Linearizing Eq. (21), one obtains

$$\delta\hat{\alpha}^{(m_1,m_2)} = -\left[\left(\frac{\partial N}{\partial\hat{\alpha}}\right)^{(m_1,m_2)}\right]^{-1} N^{(m_1,m_2)}$$
$$N^{(m_1,m_2)} = (\delta x)^2 \sum_{k=1}^{N_x-1} (\hat{\phi}_{kN_y}^{(m_1,m_2)} - \hat{\phi}_{kN_y-1}^{(m_1,m_2)} - \hat{\phi}_{k1}^{(m_1,m_2)} + \hat{\phi}_{k0}^{(m_1,m_2)}) + (\delta y)^2 \sum_{l=1}^{N_y-1} (\hat{\phi}_{N_x l}^{(m_1,m_2)} - \hat{\phi}_{N_x-1 l}^{(m_1,m_2)} - \hat{\phi}_{1l}^{(m_1,m_2)} + \hat{\phi}_{0l}^{(m_1,m_2)}) \tag{26a}$$

$$\hat{\alpha}^{(m_1,m_2+1)} = \begin{cases} \alpha^{(n-1)} & \text{if } m_1 = 0, m_2 + 1 = 0 \\ \bar{\alpha}^{(m_1-1} & \text{if } m_1 > 0, m_2 + 1 = 0 \\ \hat{\alpha}^{(m_1,m_2)} + \delta\hat{\alpha}^{(m_1,m_2)} & \text{otherwise.} \end{cases} \quad (26b)$$

In order to obtain $\tilde{\alpha}^{(m_1)}$ and $\tilde{\phi}^{(m_1)}$, the Eqs. (26) are carried out until numerical convergence is achieved, i.e.,

$$\lim_{\varepsilon_{\hat{\alpha}}^{(m_1,m_2)} \to 0} \hat{\alpha}^{(m_1,m_2)} = \tilde{\alpha}^{(m_1)}$$

$$\lim_{\varepsilon_{\hat{\phi}}^{(m_1,m_2)} \to 0} \hat{\phi}^{(m_1,m_2)} = \tilde{\phi}^{(m_1)}$$

$$\varepsilon_{\hat{\alpha}}^{(m_1,m_2)} \equiv \left\| \sqrt{\delta\hat{\alpha}^{(m_1,m_2)} \cdot \delta\hat{\alpha}^{(m_1,m_2)}} \right\|_\infty / \left\| \sqrt{\hat{\alpha}^{(m_1,m_2)} \cdot \hat{\alpha}^{(m_1,m_2)}} \right\|_\infty \quad (27)$$

$$\varepsilon_{\hat{\phi}}^{(m_1,m_2)} \equiv \left\| \sqrt{(\partial N/\partial\hat{\alpha})^{(m_1,m_2)} (\partial N/\partial\hat{\alpha})^{(m_1,m_2)}} \right\|_\infty \cdot \varepsilon_{\hat{\alpha}}^{(m_1,m_2)}.$$

Equations (26)–(27) allow one to compute the constant of integration $\tilde{\alpha}^{(m_1)}$, provided that the electrostatic potential $\hat{\phi}^{(m_1,m_2)}$ is known for all values of $m_2$ required by these equations in order for numerical convergence to be achieved. Note that in Eq. (26a), although $\partial N/\partial\hat{\alpha}$ is not known explicitly, it can be readily approximated by numerically computing $N$ at two slightly displaced values of $\hat{\alpha}$ (centered about $\hat{\alpha}^{(m_1,m_2)}$ and by forming the derivative of $N$ with respect to $\hat{\alpha}$ numerically.

Linearizing Eqs. (20), one obtains

$$e\delta\overline{\phi}^{(m_1,m_2,m_3)} - \delta\overline{n}_e^{(m_1,m_2,m_3)} \frac{\partial f}{\partial n_e}(\gamma, \overline{n}^{(m_1,m_2,m_3)}) = \hat{\alpha}^{(m_1,m_2)} - e\overline{\phi}^{(m_1,m_2,m_3)} + \frac{e^2}{4m_e c^2} \tilde{\mathbf{a}}^{(m_1)} \cdot \tilde{\mathbf{a}}^{(m_1)} + f(\gamma, \overline{n}_e^{(m_1,m_2,m_3)}) \quad (28a)$$

$$D\left[\delta\overline{\phi}^{(m_1,m_2,m_3)}\right] - 4\pi e\delta\overline{n}_e^{(m_1,m_2,m_3)} = -D\left[\overline{\phi}^{(m_1,m_2,m_3)}\right] + 4\pi e\left(\overline{n}^{(m_1,m_2,m_3)} - \sum_i Z_i n_i^{(n)}\right);$$

$$\overline{\phi}^{(m_1,m_2,m_3+1)} \equiv \begin{cases} \phi^{(n-1)} & \text{if } m_1 = 0, m_2 = 0, m_3 + 1 = 0 \\ \tilde{\phi}^{(m_1-1)} & \text{if } m_1 > 0, m_2 = 0, m_3 + 1 = 0 \\ \hat{\phi}^{(m_1,m_2-1)} & \text{if } m_1 > 0, m_2 > 0, m_3 + 1 = 0 \\ \overline{\phi}^{(m_1,m_2,m_3)} + \delta\overline{\phi}^{(m_1,m_2,m_3)} & \text{otherwise;} \end{cases}$$

$$\overline{n}_e^{(m_1,m_2,m_3+1)} \equiv \begin{cases} n_e^{(n-1)} & \text{if } m_1 = 0, m_2 = 0, m_3 + 1 = 0 \\ \tilde{n}_e^{(m_1-1)} & \text{if } m_1 > 0, m_2 = 0, m_3 + 1 = 0 \\ \hat{n}_e^{(m_1,m_2-1)} & \text{if } m_1 > 0, m_2 > 0, m_3 + 1 = 0 \\ \overline{n}_e^{(m_1,m_2,m_3)} + \delta\overline{n}_e^{(m_1,m_2,m_3)} & \text{otherwise.} \end{cases} \quad (28b)$$

In order to obtain $\hat{\phi}^{(m_1,m_2)}$ and $\hat{n}_e^{(m_1,m_2)}$, the above iterative algorithm is carried out until convergence is achieved, i.e.,

$$\lim_{\varepsilon_{\overline{\phi}}^{(m_1,m_2,m_3)} \to 0} \overline{\phi}^{(m_1,m_2,m_3)} = \hat{\phi}^{(m_1,m_2)}$$

$$\lim_{\varepsilon_{\overline{n}}^{(m_1,m_2,m_3)} \to 0} \overline{n}_e^{(m_1,m_2,m_3)} = \hat{n}_e{}^{(m_1,m_2)}$$

$$\varepsilon_{\overline{\phi}}^{(m_1,m_2,m_3)} \equiv \left\| \sqrt{\delta\overline{\phi}^{(m_1,m_2,m_3)} \delta\overline{\phi}^{(m_1,m_2,m_3)}} \right\|_\infty / \left\| \sqrt{\overline{\phi}^{(m_1,m_2,m_3)} \overline{\phi}^{(m_1,m_2,m_3)}} \right\|_\infty \quad (29)$$

$$\varepsilon_{\overline{n}}^{(m_1,m_2,m_3)} \equiv \left\| \sqrt{\delta\overline{n}_e^{(m_1,m_2,m_3)} \delta\overline{n}_e^{(m_1,m_2,m_3)}} \right\|_\infty / \left\| \sqrt{\overline{n}_e^{(m_1,m_2,m_3)} \overline{n}_e^{(m_1,m_2,m_3)}} \right\|_\infty.$$

Equations (28)–(29) allow one to compute $\hat{\phi}^{(m_1,m_2)}$ and $\hat{n}_e^{(m_1,m_2)}$.

Equations (24)–(29) represent the linearized forms of Eqs. (20)–(22). At any time level $t_n$, the quantities $\mathbf{a}^{(n-1)}$, $\phi^{(n-1)}$, $\alpha^{(n-1)}$, $n_e^{(n-1)}$, and $n_i^{(n)}$ are known, and Eqs. (24)–(29) are used to compute $\mathbf{a}^{(n)}$, $\phi^{(n)}$, $\alpha^{(n)}$, $n_e^{(n)}$ as follows:

a. Initialize $m_1$ to $-1$.

b. Set $m_1 = m_1 + 1$.

c. Initialize $m_2$ to $-1$.

d. Set $m_2 = m_2 + 1$.

e. Initialize $m_3$ to $-1$.

f. Set $m_3 = m_3 + 1$.

g. Solve Eqs. (28)–(29) for $\overline{\phi}^{(m_1,m_2,m_3)}$ and $\overline{n}_e^{(m_1,m_2,m_3)}$.

h. Check to see if Eqs. (28)–(29) have reached numerical convergence, i.e., $\varepsilon_{\overline{\phi}}^{(m_1,m_2,m_3)} < \varepsilon$ and $\varepsilon_{\overline{n}}^{(m_1,m_2,m_3)} < \varepsilon$, where $\varepsilon$ is the desired tolerance. If the convergence criteria have not been met, go back to step f.

i. Set $\hat{n}_e^{(m_1,m_2)} = \overline{n}_e^{(m_1,m_2,m_3)}$ and $\hat{\phi}^{(m_1,m_2)} = \overline{\phi}^{(m_1,m_2,m_3)}$.

j. Solve Eqs. (26)–(27) for $\hat{\alpha}^{(m_1,m_2)}$.

k. Check to see if Eqs. (26)–(27) have reached numerical convergence, i.e., $\varepsilon_{\hat{\phi}}^{(m_1,m_2)} < \varepsilon$ and $\varepsilon_{\hat{\alpha}}^{(m_1,m_2)} < \varepsilon$. If the convergence criteria have not been met, go back to step d.

l. Set $\tilde{\phi}^{(m_1)} = \hat{\phi}^{(m_1,m_2)}$, $\tilde{n}_e^{(m_1)} = \hat{n}_e^{m_1,m_2}$, and $\tilde{\alpha}^{(m_1)} = \hat{\alpha}^{(m_1,m_2)}$.

m. Solve Eqs. (24)–(25) for $\tilde{\mathbf{a}}^{(m_1)}$.

n. Check to see if Eqs. (24)–(25) have reached numeri-

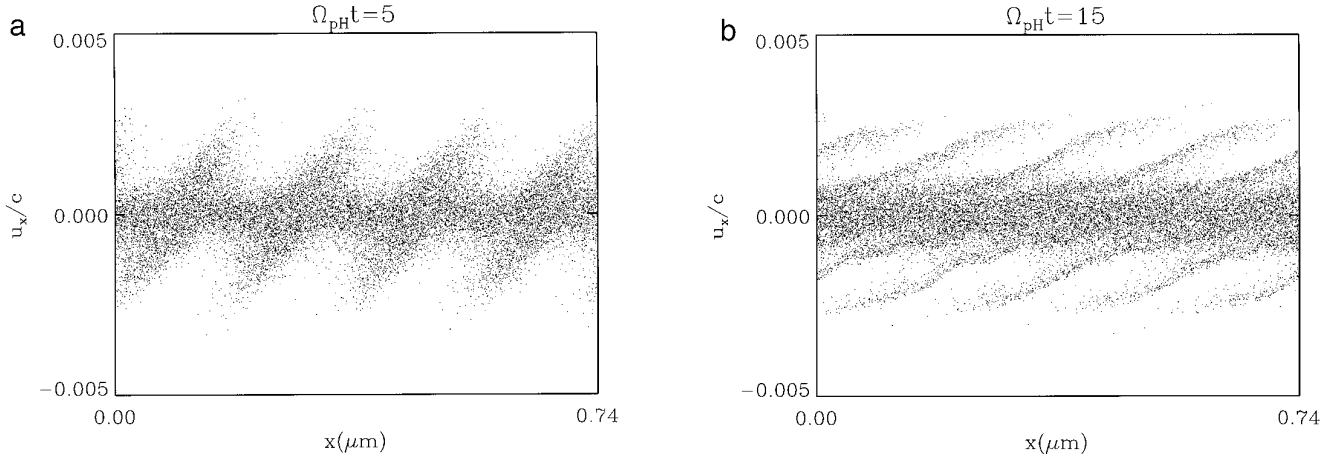


**FIG. 1.** $x - u_x$ phase space plots of: (a) protons and (b) helium ions in the absence of the pump electromagnetic wave for the case with $n_H = n_{He}$, $n_e = 8.9 \times 10^{20}$ cm$^{-3}$, $T_e = 5$ keV, $T_H = T_{He} = 0.5$ keV, $k^2\lambda_{De}^2 = 0.3523$, and $A = 0.20$. The simulation is one-dimensional.

cal convergence, i.e., $\varepsilon_{\mathbf{a}}^{(m_1)} < \varepsilon$. If the convergence criterion has not been met, go back to step b.

o. Set $\mathbf{a}^{(n)} = \tilde{\mathbf{a}}^{(m-1)}$, $\phi^{(n)} = \tilde{\phi}^{(m-1)}$, $\alpha^{(n)} = \tilde{\alpha}^{(m-1)}$, and $n_e^{(n)} = \tilde{n}_e^{(m-1)}$.

Typically, the outermost iterative algorithm requires three to four iterations to reach convergence with $\varepsilon = 10^{-6}$. For each outermost iteration, the intermediate iterative algorithm usually requires two iterations to converge.

## 4. RESULTS AND DISCUSSION

The code has been tested in one and two dimensions, and the numerical results have been compared with linear Vlasov theory. In this section, test simulations with and without the pump electromagnetic field have been performed, and the results are presented below.

### A. *Undriven Ion Acoustic Modes*

The simulations are carried out in a periodic system in which the pump wave **a** is set to zero, i.e., Eqs. (22) are not solved. Two counterstreaming ion acoustic waves having equal amplitude and wavelength are excited by imposing an initial perturbation in the ion density:

$$n_i(\mathbf{x}, t = 0) = n_{i0}[1 + A\cos(k\hat{\mathbf{e}}_x \cdot \mathbf{x})] \tag{30}$$

with no accompanying perturbation in the mean velocities of the ions. $A$, the amplitude of the initial perturbation, is the same for all ion species. For all of the test simulations, the plasma consists of two ion components, i.e., hydrogen and helium. The initial electron density $n_{e0} = \sum_i Z_i n_{i0}$ is chosen to be $8.9 \times 10^{20}$ cm$^{-3}$. This electron density corresponds to $n_{e0}/n_c = 0.1$, where $n_c$ is the critical density associated with a frequency-tripled Nd-Glass laser with vacuum wavelength $\lambda_v = 0.35$ $\mu$m. $k$, the wave number of the ion acoustic modes being excited, is taken to be $2(2\pi/\lambda_v)(1 - n_{e0}/n_c)^{1/2}$. This corresponds to the wave number of the ion acoustic wave produced in the SBS backscatter process when a high-intensity laser propagates through a plasma with $n_e/n_c = 0.1$.

The subsequent evolution of the excited ion acoustic waves can be expressed as

$$n_i(\mathbf{x}, t) = n_{i0}[1 + \tfrac{1}{2}Ae^{\omega_I t}(\cos(k\hat{\mathbf{e}}_x \cdot \mathbf{x} - \omega_R t) + \cos(k\hat{\mathbf{e}}_x \cdot \mathbf{x} + \omega_R t))], \tag{31}$$

where $\omega = \omega_R + i\omega_I$ is the frequency of the ion acoustic modes and can be obtained from linear Vlasov theory. $\omega_I$ is the Landau damping of the ion acoustic waves. The total energy carried by the waves can be shown to be of the form

$$E \propto \int \sum_i Z_i^2[n_i(\mathbf{x}, t) - n_{i0}]^2 \, d^3\mathbf{x}.$$

Substituting Eq. (31) into the above equation, one obtains the following expression for the wave energy:

$$E = \frac{E_0}{2} e^{2\omega_I t}[1 + \cos(2\omega_R t)]. \tag{32}$$

Thus, by examining the total energy carried by the wave as a function of time, one can extract both the real and the imaginary parts of the frequency $\omega$ from the particle-in-cell simulations. The observed frequency $\omega$ can then be compared with linear Vlasov theory. It should be noted here that we have intentionally excited two counterstreaming ion acoustic waves so that the total wave energy will exhibit both the damping and the oscillatory behavior. If

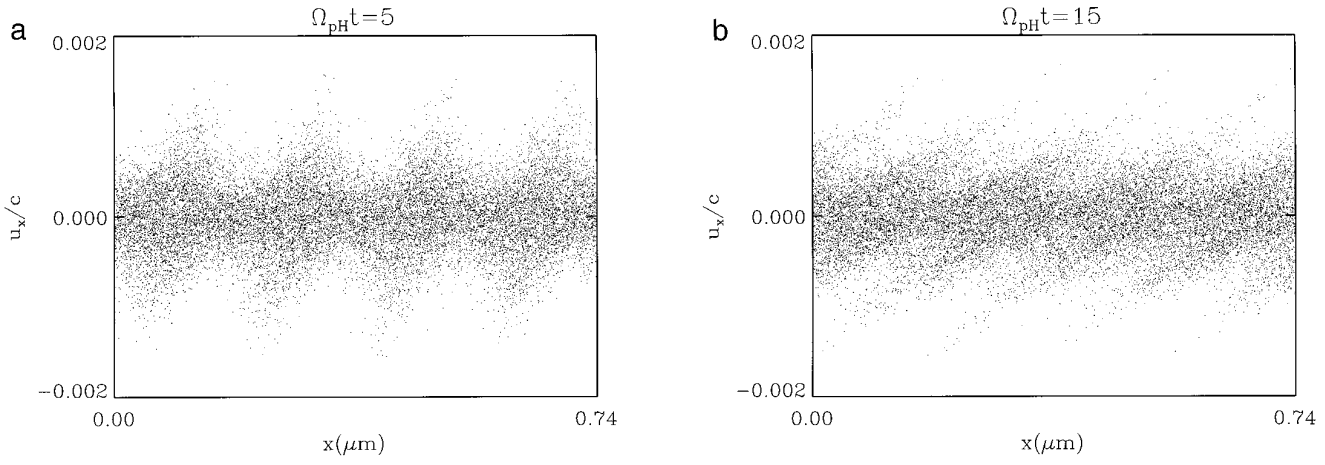


**FIG. 2.** $x - u_x$ phase space plots of: (a) protons and (b) helium ions for the same simulation described in Figs. 1, but at a later time ($\Omega_{pH}t = 15$).

only one ion acoustic wave were excited, the total wave energy would only exhibit the damping behavior, and the real part of the wave frequency cannot be extracted readily from the simulation results.

First, a one-dimensional simulation was performed in which the plasma consists of protons and helium ions with $n_H = n_{He} = n_e/3$, $T_e = 5$ keV, and $T_H = T_{He} = 0.5$ keV. For this simulation, $(k\lambda_{De})^2 = 0.3523$. The length of the simulation box is $L = 0.7392\ \mu$m (the length $L$ normalized to the proton inertial length is $L/(c/\Omega_{pH}) = 0.05525$) and corresponds to four ion acoustic wavelengths. The ratio of electron specific heats, $\gamma$, is taken to be 1. The initial amplitude of perturbation $A$ is chosen to be 0.2. The simulation box has 100 computational cells, and each ion species is represented by 200 particles per cell. For this simulation, $\Omega_{pH}\delta t = 0.1$, where $\Omega_{pH}$ is the proton plasma frequency.

Figures 1 and 2 are phase-space plots ($x - u_x$) of the protons and helium ions at $\Omega_{pH}t = 5, 15$. Figures 1 and 2 reveal two prominent features. First, there are indeed two counterstreaming ion acoustic waves as expected. Second, the proton distribution is much more strongly perturbed by the ion acoustic waves than the helium ion distribution. This is also expected because the protons have a higher thermal speed and, therefore, can exchange energy resonantly with the ion acoustic waves more effectively [29]. The process by which the ions in the high-energy tail of the distributions are accelerated, as is evident from Figs. (1)–(2), is known as Landau damping of the ion acoustic waves. Figure 3 is a time history of the electric field energy (solid line) from which the numerically observed frequency of the ion acoustic waves, $\omega_N$, is estimated to be $\omega_N/\Omega_{pH}$

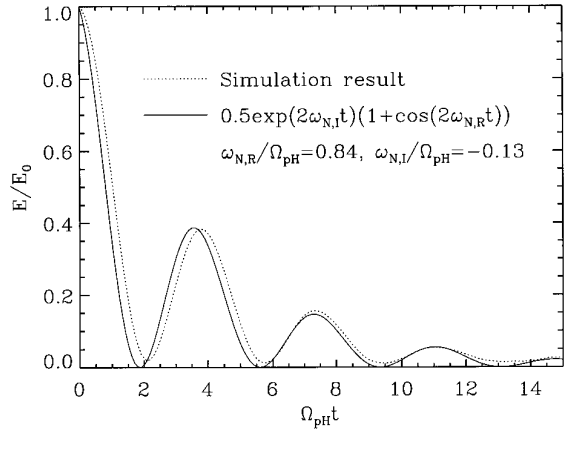


**FIG. 3.** Time history of the normalized electric field energy (solid line) for the simulation described in Figs. 1. The dashed line represents an analytic fit from which the numerically observed ion acoustic frequency is determined to be $\omega_N/\Omega_{pH} = 0.84–0.13i$.

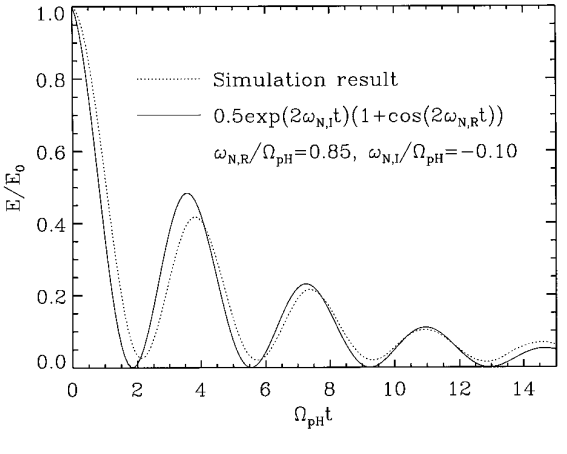


**FIG. 4.** Time history of the normalized electric field energy (solid line) for a one-dimensional simulation of the case described in Figs. 1, but with a smaller amplitude of initial density perturbation ($A = 0.05$). The dashed line represents an analytic fit from which the numerically observed ion acoustic frequency is determined to be $\omega_N/\Omega_{pH} = 0.85–0.10i$.

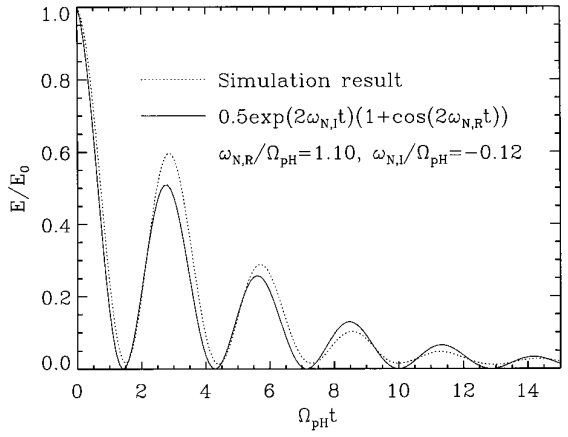


**FIG. 5.** Time history of the normalized electric field energy (solid line) for a two-dimensional simulation with $n_H = n_C$, $n_e = 8.9 \times 10^{20}$ cm$^{-3}$, $T_e = 5$ keV, $T_H = T_{He} = 0.5$ keV, $k^2\lambda_{De}^2 = 0.3523$, and $A = 0.20$. The dashed line represents an analytic fit from which the numerically observed ion acoustic frequency is determined to be $\omega_N/\Omega_{pH} = 1.10–0.12i$.

$= 0.84–0.13i$. The dashed line represents an analytic curve of the form $E_{fit}/E_0 = 0.5e^{2\omega_{N,I}t}\ (1 + \cos(2\omega_{N,R}t))$. The expected frequency of the ion acoustic waves, determined by solving the linear Vlasov dispersion relation, is $\omega/\Omega_{pH} = 0.91–0.08i$ [30]. The difference between $\omega_N$ and $\omega$ is due to the fact that the ion acoustic waves excited in the simulation are in fact not linear ($A = 0.2$). This is confirmed when a second simulation was performed for which $A = 0.05$. In this case, each ion species is represented by 2000 particles per cell. The time history of the electric field energy is shown in Fig. 4. The resulting numerically observed frequency is estimated to be $\omega_N/\Omega_{pH} = 0.85–0.10i$ and is in much closer agreement with linear Vlasov theory. In principle, one can reduce $A$ sufficiently to obtain exact agreement between $\omega_N$ and $\omega$. However, such a simulation would be prohibitively expensive because the number of finite-size particles in the system would need to increase in proportion with $1/A^2$ in order to keep statistical fluctuations at acceptable levels.

Next, a one-dimensional simulation was performed in which the plasma consists of protons and carbon ions with $n_H = n_C = n_e/7$. The initial amplitude of perturbation, $A$, is chosen to be 0.05. Each ion species is represented by 2000 particles per computational cell. All other parameters corresponds to those of Figs. 1–3. The phase-space plots ($x - u_x$) for this simulation show the same features as those of Figs. 1–2, and are therefore not shown. Figure 5 shows the time history of the electric field energy (solid line). The numerically observed frequency is estimated to be $\omega_N/\Omega_{pH} = 1.10–0.12i$. The expected frequency of the ion acoustic waves, determined by solving the linear Vlasov dispersion relation, is $\omega/\Omega_{pH} = 1.16–0.143i$ [30]. Here, the simulation results are in good agreement with linear Vlasov theory.

Last, a two-dimensional simulation was performed in which the plasma is identical to that of Figs. 1–3. The length and width of the simulation box are $L_x = 0.7392$ $\mu$m and $L_y = L_x/5$, respectively. The computation mesh consists of $100 \times 20$ cells. Each ion species is represented by 200 particles per computational cell. Figures 6 and 7 are phase-space plots ($x - u_x$ and $y - u_y$) of the protons and helium ions, respectively, at $\Omega_{pH}t = 15$. Figures 6 and 7 indicate that the ion acoustic waves excited in the simulation box are indeed one-dimensional; i.e., there is no scattering of the ion acoustic waves. Figure 8 shows the time history of the electric field energy (solid line). The numerically observed frequency is estimated to be $\omega_N/\Omega_{pH} = 0.84–0.13i$, consistent with results from the previous one-dimensional simulation.

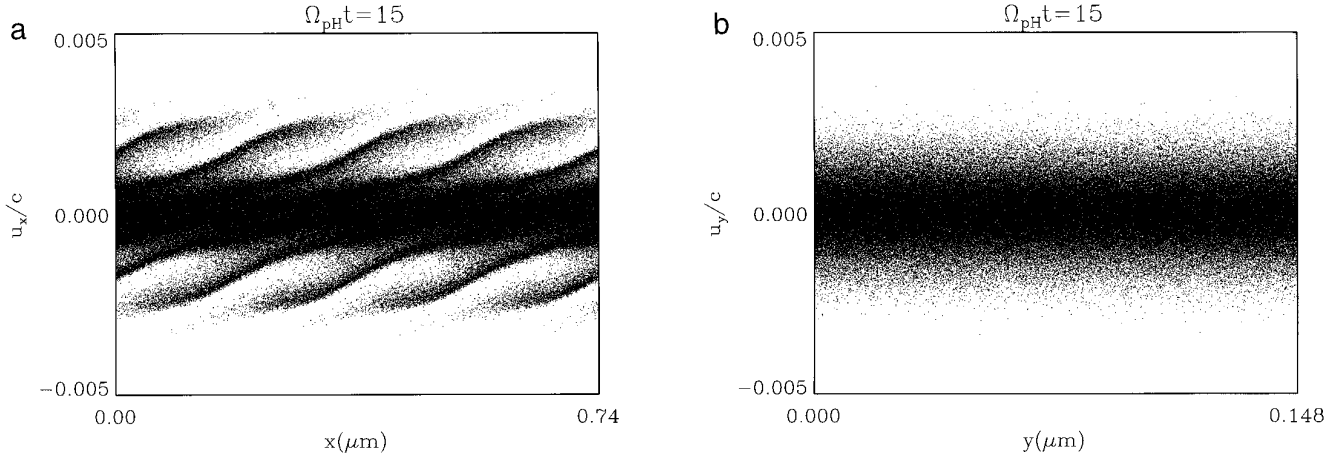


**FIG. 6.** $x - u_x$ phase space plots of: (a) protons and (b) helium ions for a two-dimensional simulation with $n_H = n_{He}$, $n_e = 8.9 \times 10^{20}$ cm$^{-3}$, $T_e = 5$ keV, $T_H = T_{He} = 0.5$ keV, $k^2\lambda_{De}^2 = 0.3523$, and $A = 0.20$. Note that this is that same case as described in Figs. 1.

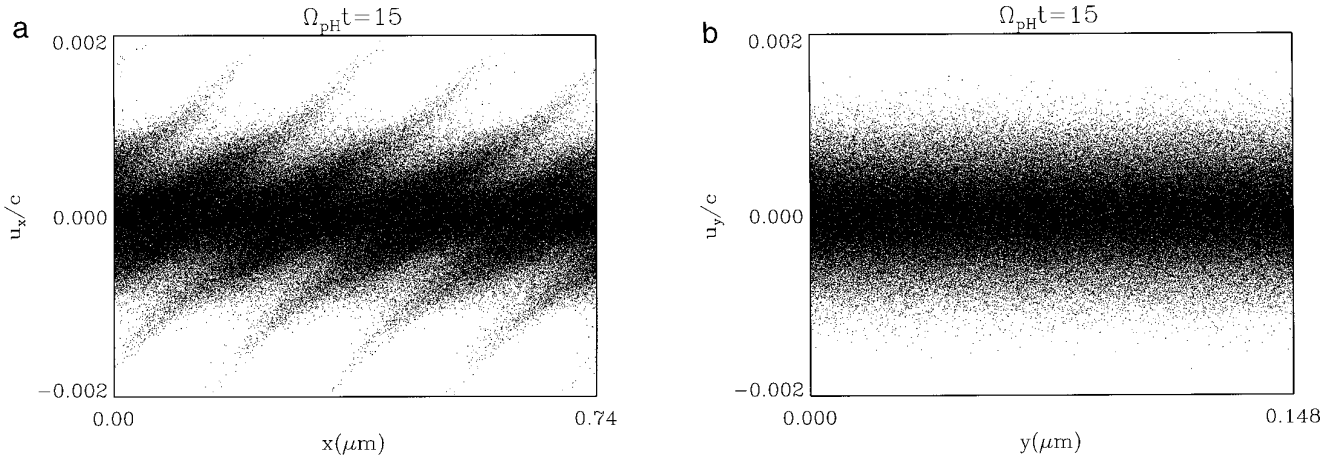


**FIG. 7.** $y - u_y$ phase space plots of: (a) protons and (b) helium ions of the two-dimensional simulation described in Figs. 6. The phase space plots indicate that the ion acoustic waves remain one-dimensional even at late time.

B. *Aperiodically Driven SBS Simulations*

The simulations are performed in a rectangular simulation box ($0 \le x \le L_x$ and $0 \le y \le L_y$) with periodic boundary conditions in the $y$ direction and aperiodic boundary conditions in the $x$ direction. The electromagnetic pump wave enters left boundary ($x = 0$), and exits the right boundary ($x = L_x$). In addition to the periodicity in the $y$ direction, the boundary conditions for $\phi$ and $\mathbf{a}$ are

$$\begin{aligned}
\phi(0, y, t) &= 0 \\
\hat{\mathbf{e}}_x \cdot \nabla\phi(L_x, y, t) &= 0 \\
\hat{\mathbf{e}}_x \cdot \nabla\mathbf{a}(0, y, t) &= iK(0, y, t)(2\mathbf{a}_0 - \mathbf{a}(0, y, t)) \\
\hat{\mathbf{e}}_x \cdot \nabla\mathbf{a}(L_x, y, t) &= -iK(L_x, y, t)(2\mathbf{a}_s \exp(i\Delta\omega t) \\
&\quad - \mathbf{a}(L_x, y, t)).
\end{aligned}$$

Here, $\mathbf{a}_0$ and $\mathbf{a}_s$ are input quantities and correspond to the incident electromagnetic wave on the left boundary and the reflected electromagnetic wave on the right boundary. $\mathbf{a}_0$ is related to the incident laser intensity I as follows:

$$\mathbf{a}_0 \cdot \mathbf{a}_0^* = \left(\frac{8\pi}{c\omega_0^2}\right) \mathrm{I}.$$

Physically, $\mathbf{a}_s$ represents the electromagnetic perturbation from which the parametric three-wave coupling process, i.e., SBS in this particular case, will grow. For the simulations shown in this section, $\mathbf{a}_s$ is taken to be $10^{-4}\mathbf{a}_0$. $\Delta\omega$ is the frequency difference between the incident and the scattered electromagnetic waves. The frequency matching condition at resonance is $\Delta\omega_{\mathrm{res}} = \omega_{\mathrm{R}}$, where $\omega_{\mathrm{R}}$ is the frequency of the ion acoustic mode with wavenumber $2K_0$, i.e., the ion acoustic mode simulated in Section 4A. The simulations to be discussed below are performed at resonance.

Initially, the plasma is spatially uniform. The initial condition for $\mathbf{a}$ is

$$\mathbf{a}(x, y, 0) = \mathbf{a}_0 \exp(iK_0x) + \mathbf{a}_s \exp(-iK_0x),$$

where $K_0 \equiv K(x, y, 0)$ is simply a constant.

First, a one-dimensional simulation was performed in which the plasma consists of protons and helium ions with $n_{\mathrm{H}} = n_{\mathrm{He}} = n_e/3$, $T_e = 5$ keV, and $T_{\mathrm{H}} = T_{\mathrm{He}} = 0.5$ keV. The electron density $n_e$ is taken to be $8.9 \times 10^{20}$ cm$^{-3}$. Note that these plasma conditions are the same as those of Figs. 1–3. For this simulation, $L_x = 10$ $\mu$m. The ratio of specific heats, $\gamma$, is taken to be 1. $\omega_0$ is taken to be

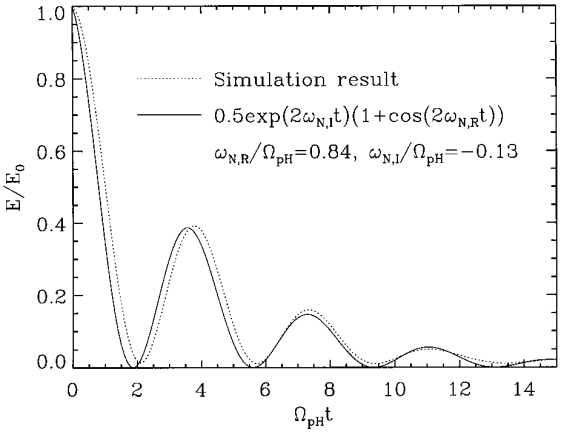


**FIG. 8.** Time history of the normalized electric field energy (solid line) for the simulation described in Figs. 6. The dashed line represents an analytic fit from which the numerically observed ion acoustic frequency is determined to be $\omega_{\mathrm{N}}/\Omega_{p\mathrm{H}} = 0.84–0.13i$.

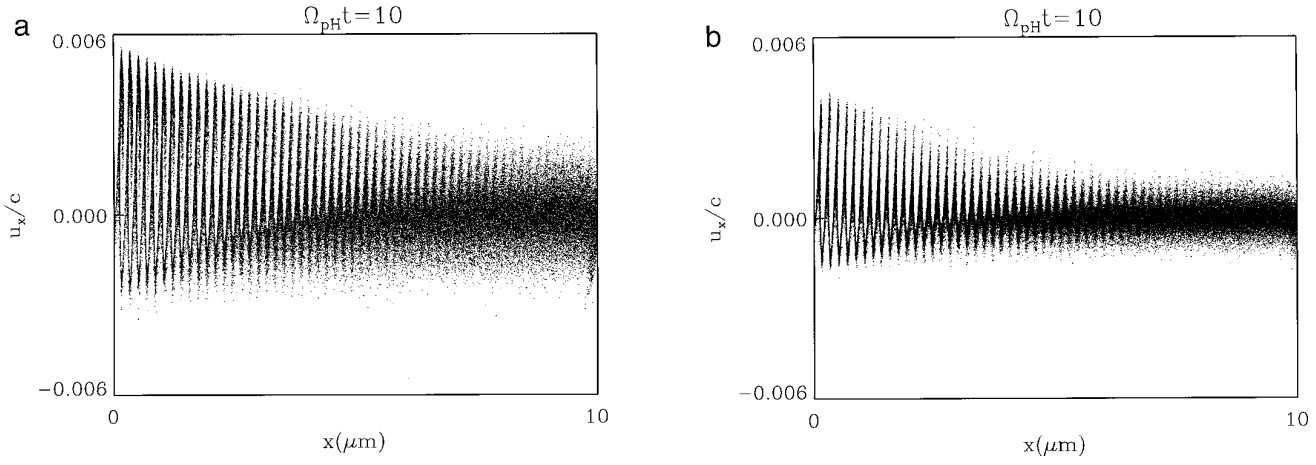


**FIG. 9.** $x - u_x$ phase space plots of: (a) protons and (b) helium ions in the presence of a frequency-tripled Nd-Glass laser pump wave with intensity $I = 5 \times 10^{17}$ W/cm$^2$ for the case with $n_H = n_{He}$, $n_e = 8.9 \times 10^{20}$ cm$^{-3}$, $T_e = 5$ keV, $T_H = T_{He} = 0.5$ keV, $k^2\lambda_{De}^2 = 0.3523$. The simulation is one-dimensional.

$5.37 \times 10^{15}$ Hz and corresponds to a frequency-tripled Nd–Glass laser with vacuum wavelength $\lambda_v = 0.351$ $\mu$m. I, the intensity of the incident pump wave, is $5 \times 10^{17}$ W/cm$^2$. The simulation box has 800 computational cells, and each ion species is represented by 200 particles per cell. For this simulation, $\Omega_{pH}\delta t = 0.2$, where $\Omega_{pH}$ is the proton plasma frequency. Because of the fact that the simulation is performed in one dimension, the only three-wave parametric processes that can be excited are the backward and forward SBS processes. Theoretically, the backward scattering process is expected to dominate over the forward scattering process [22]. Figures 9 are phase-space plots $(x - u_x)$ of the protons and helium ions at $\Omega_{pH}t = 10$. Figures 9 indicate that both the protons and helium ions are strongly driven and that particle trapping is evident for the protons. The wavelength of the ion acoustic wave is about half that of the pump electromagnetic wave, as is expected for backward SBS. Figure 10 is a time history plot of the total kinetic energy of the ions normalized to the initial thermal energy. The dashed line, whose slope yields the energy growth rate, is superimposed on the time history plot for clarity. The normalized growth rate for the dominant stimulated Brillouin scattering mode, $\omega_{SBS}/\Omega_{pH}$, is determined from Fig. 10 to be 0.177. It should be mentioned that an identical simulation, but with only 50 particles per cell for each ion species, yields the same growth rate.

Next, a two-dimensional simulation is perfomed in which plasma condition and incident laser intensity are identical to those of the above one-dimensional simulation, except for the fact that each ion species is represented by only 50 particles per cell. $L_y$, the spatial extent of the plasma in the $y$ direction, is 10 $\mu$m, i.e., $L_y = L_x$. There are 50 computational cells in the $y$ direction. Figures 11 are contour plots of $\mathbf{a}(k_x, k_y) \cdot \mathbf{a}^*(k_x, k_y)$ at $\Omega_{pH}t = 10, 30$. Although backscatter is dominant at early time (cf. Fig. 11a), there is evidence of strong sidescatter at late time, as can be seen in Fig. 11b. The time history of the normalized total kinetic energy of the ions is shown in Fig. 12. Comparing Fig. 12 to Fig. 10 indicates that the growth rate in one and two dimensions are comparable for the present simulation. Finally, particle plots in configuration space of protons and helium ions at $\Omega_{pH}t = 30$, Fig. 13, show that at late time, the plasma has strongly filamented.

For the one- and two-dimensional simulations presented above, $\omega_0/\Omega_{pH}$, the frequency of the driving electromagnetic field normalized to the proton plasma frequency, is 236. Therefore, for these particular cases, our hybrid PIC

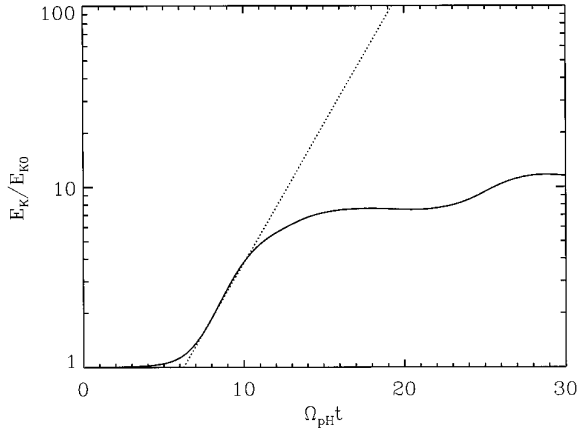


**FIG. 10.** Time history of the normalized particle kinetic energy (solid line) for the simulation described in Figs. 9. The dashed line represents the straight line whose slope yields the numerically observed SBS growth rate $\omega_{SBS}/\Omega_{pH} = 0.177$.

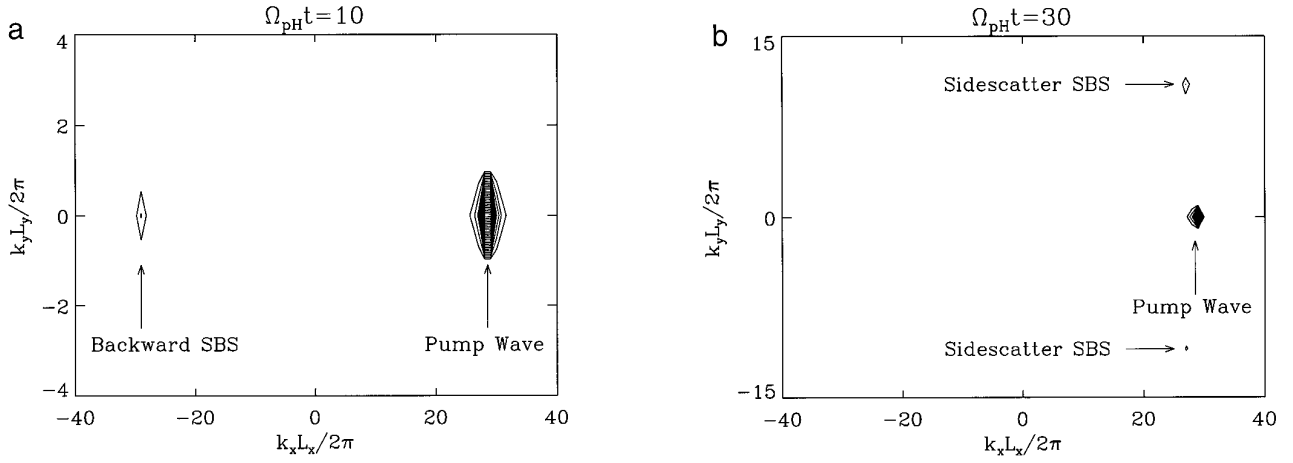


**FIG. 11.** Contour plots of the power spectrum of the vector potential, $\mathbf{a}(k_x, k_y) \cdot \mathbf{a}^*(k_x, k_y)$, at $\Omega_{pH}t = 10, 30$ for a two-dimensional simulation of the same case described in Figs. 9.

method allows a time step two orders of magnitude larger than that allowed by explicit PIC methods that require the time scale of the driving electromagnetic field to be resolved.

## 5. SUMMARY AND CONCLUSIONS

In this report, a particle-in-cell model appropriate for describing ion-driven parametric instabilities in laser-driven plasmas is presented. The model, based on a temporal WKB analysis of the electromagnetic field equations and on the time-averaged electron fluid momentum equation, is inherently nonlinear because of the dependence of the electron response on the energy density of the electromagnetic wave. The model consists of a Schrodinger-like equation for the vector potential, Poisson's equation for the scalar potential, an exactly-integrable electron momentum equation, and the equations of motion for the finite-size ion particles. A splitting algorithm based on the standard Newton–Raphson method is proposed for solving the coupled nonlinear equations. Both the particle-in-cell model and the splitting algorithm are independent of the number of spatial dimensions and have been implemented in one- and two-dimensional geometries. Both the temporal and spatial differencing schemes are discussed in detail. A nonlinear stability analysis of the temporal differencing scheme is also discussed.

Both one- and two-dimensional test simulations with and without the pump electromagnetic field have been performed. Of particular interest is the ion Landau damping process in which ion acoustic waves are damped even in the absence of collisional dissipation. Also of interest is the stimulated Brillouin scattering process in which a pump electromagnetic wave decays into a low-frequency ion acoustic wave and a scattered electromagnetic wave. When the pump electromagnetic wave is of sufficient intensity, both the ion acoustic wave and the scattered electromagnetic wave are amplified at the expense of the pump electromagnetic wave. Although the test simulations have been focused on Landau damping and stimulated Brillouin scattering, a wide range of ion-driven parametric instabilities can be simulated by the particle-in-cell model presented in this report.

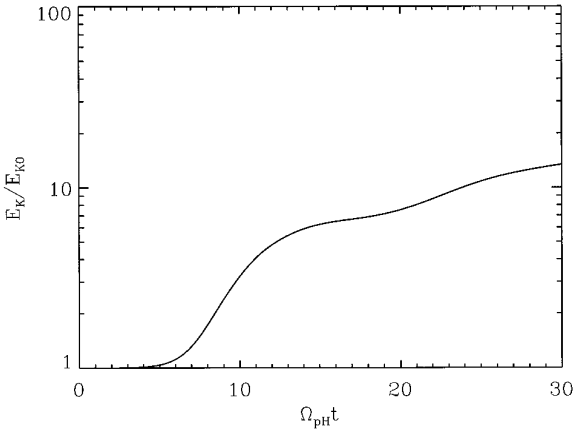


**FIG. 12.** Time history of the normalized particle kinetic energy (solid line) for the simulation described in Figs. 11. The observed SBS growth rate is nearly identical to that seen in the one-dimensional simulation described in Figs. 9.

## ACKNOWLEDGMENTS

This work was supported by the Inertial Confinement Fusion Theory and Design Program at Los Alamos. The author thanks Drs. J. M. Wallace and B. Bezzerides for many helpful suggestions and invigorating discussions.

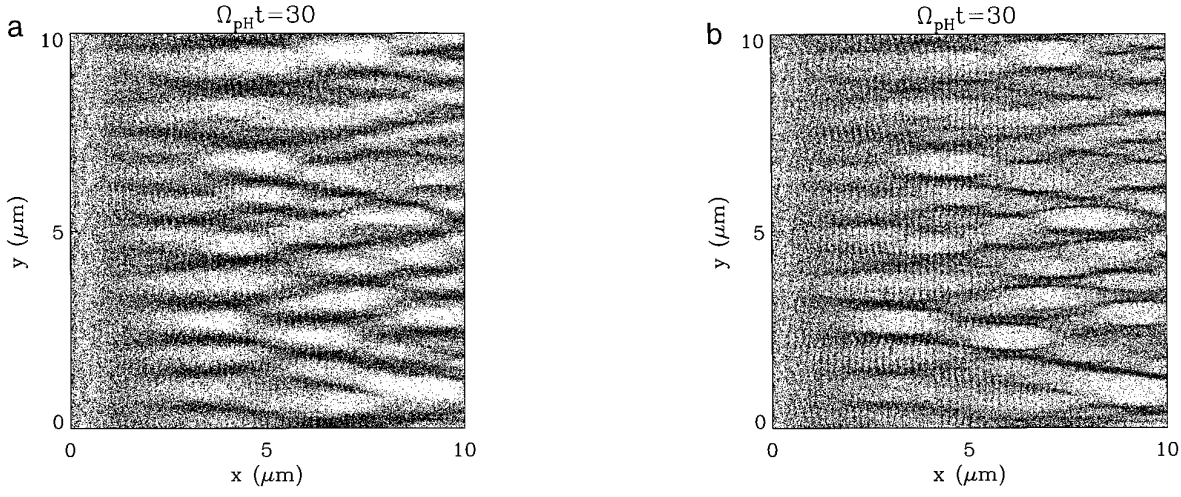


**FIG. 13.** Particle plots in configuration space of: (a) protons and (b) helium ions for the simulation described in Figs. 9 at $\Omega_{pH}t = 30$. The plasma has strongly filamented by this time.

## REFERENCES


1. J. M. Dawson, *Rev. Mod. Phys.* **55,** 403 (1983).
2. H. X. Vu and J. U. Brackbill, *Comput. Phys. Commun.* **69,** 253 (1992).
3. J. U. Brackbill and D. W. Forslund, *J. Comput. Phys.* **46,** 271 (1982).
4. D. W. Forslund and J. U. Brackbill, *Phys. Rev. Lett.* **48,** 1614 (1982).
5. J. U. Brackbill and D. W. Forslund, in *Computational Techniques: Multiple Time Scales,* edited by J. U. Brackbill and B. I. Cohen (Academic Press, Orlando, FL, 1985).
6. D. Dickman, R. L. Morse, and C. W. Nielson, *Phys. Fluids* **12,** 1708 (1969).
7. A. B. Langdon, *J. Comput. Phys.* **6,** 247 (1970).
8. A. B. Langdon and B. F. Lasinski, *Methods Comput. Phys.* **16,** 327 (1976).
9. C. W. Nielson and H. R. Lewis, *Methods Comput. Phys.* **16,** 367 (1976).
10. J. Busnardo-Neto, P. L. Pritchett, A. T. Lin, and J. M. Dawson, *J. Comput. Phys.* **23,** 300 (1977).
11. J. A. Byers, B. I. Cohen, W. C. Condit, and J. D. Hanson, *J. Comput. Phys.* **27,** 363 (1978).
12. D. W. Hewett and C. W. Nielson, *J. Comput. Phys.* **29,** 219 (1978).
13. D. W. Hewett, *J. Comput. Phys.* **38,** 378 (1980).
14. R. J. Mason, *J. Comput. Phys.* **41,** 233 (1981).
15. J. Denavit, *J. Comput. Phys.* **42,** 337 (1981).
16. R. J. Mason, in *Computational Techniques: Multiple Time Scales,* edited by J. U. Brackbill and B. I. Cohen (Academic Press, Orlando, FL, 1985).
17. B. I. Cohen, in *Computational Techniques: Multiple Time Scales,* edited by J. U. Brackbill and B. I. Cohen (Academic Press, Orlando, FL, 1985).
18. A. B. Langdon and D. C. Barnes, in *Computational Techniques: Multiple Time Scales,* edited by J. U. Brackbill and B. I. Cohen (Academic Press, Orlando, FL, 1985).
19. R. W. Hockney and J. W. Eastwood, *Computer Simulation Using Particles* (Adam Hilger, New York, 1988).
20. H. X. Vu, J. U. Brackbill, and D. Winske, *J. Geophys. Res.* **97,** 13839 (1992).
21. J. U. Brackbill and H. X. Vu, *Geophys. Res. Lett.* **20,** 2015 (1993).
22. W. L. Kruer, *The Physics of Laser Plasma Interactions* (Addison–Wesley, New York, 1988).
23. D. W. Forslund, J. M. Kindel, and E. L. Lindman, *Phys. Fluids* **18,** 1017 (1975).
24. A. Ghizzo, T. Reveille, P. Bertrand, T. W. Johnson, J. Lebas, and M. Shouchri, *J. Comput. Phys.* **118,** 356 (1995).
25. K. Estabrook, S. C. Wilks, W. L. Kruer, J. Denavit, D. E. Hinkle, D. Kalantar, A. B. Langdon, B. J. Macgowan, D. Montgomery, J. Moody, and E. A. Williams, *Bull. Am. Phys.* **39,** 1733 (1994).
26. S. C. Wilks, W. L. Kruer, R. L. Berger, E. A. Williams, and J. Denavit, "Studies of Stimulated Brillouin Scattering Using a Hybrid Particle Ion/Fluid Electron Code," in *Proceedings, Twenty Second Annual Anomalous Absorption Conference, Lake Placid, NY, July 1992.*
27. B. Bezzerides, D. W. Forslund, and E. L. Lindman, *Phys. Fluids* **21,** 2179 (1978).
28. J. M. Ortega and W. C. Rheinboldt, *Iterative Solution of Nonlinear Equations in Several Variables* (Academic Press, New York, 1970).
29. B. D. Fried, R. B. White, and T. K. Samec, *Phys. Fluids* **14,** 2388 (1971).
30. H. X. Vu, J. M. Wallace, and B. Bezzerides, *Phys. Plasmas* **1,** 3542 (1994).